

Mapping "Brain Coral" Regions on Mars using Deep Learning

KYLE A. PEARSON^{ID},¹ ELDAR NOE,² DANIEL ZHAO,³ ALPHAN ALTINOK,¹ AND ALEX MORGAN²

¹*Jet Propulsion Laboratory, California Institute of Technology, Pasadena, CA 91125 USA*

²*Planetary Science Institute, Moffett Field, CA, 94035 USA*

³*California Institute of Technology, Pasadena, CA 91125 USA*

ABSTRACT

One of the main objectives of the Mars Exploration Program is to search for evidence of past or current life on the planet. To achieve this, Mars exploration has been focusing on regions that may have liquid or frozen water. A set of critical areas may have seen cycles of ice thawing in the relatively recent past in response to periodic changes in the obliquity of Mars. In this work, we use convolutional neural networks to detect surface regions containing "Brain Coral" terrain, a landform on Mars whose similarity in morphology and scale to sorted stone circles on Earth suggests that it may have formed as a consequence of freeze/thaw cycles. We use large images (\sim 100-1000 megapixels) from the Mars Reconnaissance Orbiter to search for these landforms at resolutions close to a few tens of centimeters per pixel (\sim 25–50 cm). Over 52,000 images (\sim 28 TB) were searched (\sim 5% of the Martian surface) where we found detections in 201 images. To expedite the processing we leverage a classifier network (prior to segmentation) in the Fourier domain that can take advantage of JPEG compression by leveraging blocks of coefficients from a discrete cosine transform in lieu of decoding the entire image at the full spatial resolution. The hybrid pipeline approach maintains \sim 93% accuracy while cutting down on \sim 95% of the total processing time compared to running the segmentation network at the full resolution on every image. The timely processing of big data sets helps inform mission operations, geologic surveys to prioritize candidate landing sites, avoid hazardous areas, or map the spatial extent of certain terrain. The segmentation masks and source code are available on GitHub^{a)} for the community to explore and build upon.

Keywords: Mars – Remote sensing – Convolutional Neural Networks

1. INTRODUCTION

Brain coral is a geologically young terrain that has the potential to enhance our understanding on the role of water in the recent geological history of Mars. "Brain coral" is a descriptive term given to a decameter-scale surface texture on Mars that consists of labyrinthine ridges and troughs occurring in flat terrains, typically in topographic lows. It is found primarily at mid-latitudes and is often associated with lineated valley fill (LVF), concentric crater fill (CCF) and lobate debris aprons (LDA) (e.g., Squyres 1978; Malin & Edgett 2001; Carr 2001; Mangold 2003). This terrain type shares morphological similarities to sorted stone circles on Earth, which are thought to form as the result of numerous freeze/thaw cycles of rock-bearing soil (Noe Dobrea et al. 2007). In Earth's arctic environments, sorted stone circles and labyrinthins are the result of a rock-bearing and water-rich soil layer that undergoes heave/contraction cycles as the result of freezing-thaw processes (Taber 1929; Taber 1930; Williams et al. 1989) whereby rock-soil segregation can systematically occur (Konrad & Morgenstern 1980) and lead to pattern formation (e.g. Werner 1999; Kessler & Werner 2003). The convective kinematics of this process are reasonably well explored (Goldthwait 1976; Williams et al. 1989) through the analysis of trenches and seasonal data from tilt meters and other field studies (e.g. Hallet & Waddington 2020). However, while the morphologies of brain coral and sorted stone circles are similar, similarity in form does not necessarily imply the same underlying process. Competing hypotheses argue brain coral formed by sublimation lag, polygon inversion, or stone sorting by freeze-thaw (Mangold 2003; Noe Dobrea et al. 2007; Levy et al. 2009), but

^{a)} <https://github.com/pearsonkyle/Mars-Brain-Coral-Network>

its origin remains unresolved. Multiple classes of young geomorphic features on Mars suggest that thawing may have occurred in the recent geologic past and may still be ongoing, although significant controversy remains McEwen et al. (2011). It is therefore important to compare available hypotheses (Mangold 2003, Milliken et al. 2003, Costard et al. 2002 and Kreslavsky et al. 2008) by performing a careful and detailed study of this terrain.

Sorted stone circles on Earth are thought to form from cyclic freezing and thawing in permafrost regions, which drives the convection of stones, soil, and water in the active layer (Mangold 2005). In western Spitsbergen, the stone circles consist of a central 2-3 m wide plug of soil surrounded by a 0.5-1 m wide ring of stones, with the plug domed up to 0.1 m and the stones rising up to 0.5 m (Kessler et al. 2001). Though stones are often cm-scale, meter-sized clasts in circles up to 20 m across occur as well (Trombotto 2000; Balme et al. 2009). Comparatively, brain coral cells on Mars measure ~5-15 m with ridges 0.2-2 m tall, resembling terrestrial circles in scale (Kessler et al. 2001; Kääb et al. 2014). On Mars, brain coral terrain is relatively young based on crater counts (Morgan et al. *in prep*), though rigorous analysis is still needed.

The Mars Reconnaissance Orbiter (MRO) has collected images of the Martian surface for over 15 years and amassed over 50 terabytes of data. The High Resolution Imaging Science Experiment (HiRISE; 0.3 m/pixel resolution; McEwen et al. 2007) and the Context Camera (CTX; 6 m/pixel resolution; Malin & Edgett 2001) are two instruments onboard MRO that are routinely used to study geological landforms. The total volume of data from this mission poses new challenges for the planetary remote-sensing community. For example, each image includes limited metadata about its content, and it is time-consuming to manually analyze each image by eye. Therefore, there is a need for computational techniques to search the HiRISE and CTX image databases and discover new content.

Many algorithms can classify image content, often requiring preprocessing like edge detection or histogram of oriented gradients (Dalal & Triggs 2005). Image compression relies on frequency domain transforms like discrete cosine transforms in JPEG to remove redundant data. Recently, deep learning approaches have utilized these compressed representations for efficient near state-of-the-art object classification (Russakovsky et al. 2015; Gueguen et al. 2018; Chamain & Ding 2019). Convolutional neural networks (CNNs) can now match human performance in object recognition tasks making them an excellent choice for an algorithm capable of learning optimal features from training data (He et al. 2015; Ioffe & Szegedy 2015). For planetary mapping, CNNs outperform other classifiers like support vector machines Palafox et al. 2017, and can be fine-tuned to identify landforms in Martian images (Wagstaff et al. 2018; Nagle-McNaughton et al. 2020). Other relevant approaches for planetary exploration include terrain segmentation to inform navigation (Dai et al. 2022) and caption generation for planetary images (Qiu et al. 2020). Leveraging frequency domain data saves significant time when processing large archives by avoiding full decoding. This enables timely surveys to inform landing site selection and identify rare features like potential astrobiology targets.

We are interested in automating the detection of brain coral terrain with images from MRO/HiRISE. To expedite the processing we leverage a classifier network (prior to segmentation) in the Fourier domain that can take advantage of JPEG compression by leveraging blocks of coefficients from a discrete cosine transform in lieu of decoding the entire image at the full spatial resolution. The hybrid pipeline approach cuts down on the total processing time compared to running a segmentation network at the full resolution on every image. In the sections below we will discuss how the training data is made, what goes into each of the networks we tested, and then quantify the performance and accuracy of predicting brain coral terrain.

2. OBSERVATIONS AND TRAINING DATA

We analyze observations of the Martian surface using the High Resolution Imaging Science Experiment onboard the Mars Reconnaissance Orbiter (MRO) (McEwen et al. 2007). Images from the primary and extended mission were used and are publicly available online¹. HiRISE has a 0.5 m telescope along with an optical camera however for the purposes of our study we use images from the red channel which has a photometric range between ~550–800 nm. The MRO spacecraft orbits Mars at an altitude of around 300 km and depending on the pointing, the HiRISE camera is capable of imaging the surface at resolutions between ~25-50 cm/px. The camera reads swaths of data at a time tracking the ground in spans of 20,000 pixels and combined images are usually 100,000's pixels long. The vast amount of image data is stored with 10-bit precision as a JPEG2000 image. The image encoding algorithm is capable of compressing images to ~5-10% their original size, e.g., 10.8 GB of data at the full spatial resolution (*ESP_036917_2210*) compresses into as little as ~675 MB of space on disk. Decoding images at the full-resolution can often take up to a few minutes

¹ <https://hirise.lpl.arizona.edu/>

90 on a CPU depending on the image size (see Figure 1). The HiRISE archive contains over 28 TB of compressed data
 91 spanning over 52,000 images from their primary and extended mission with data still being acquired. Processing
 92 terabytes worth of images requires spending a non-negligible time decoding the data alongside applying any computer
 93 vision algorithm afterward.

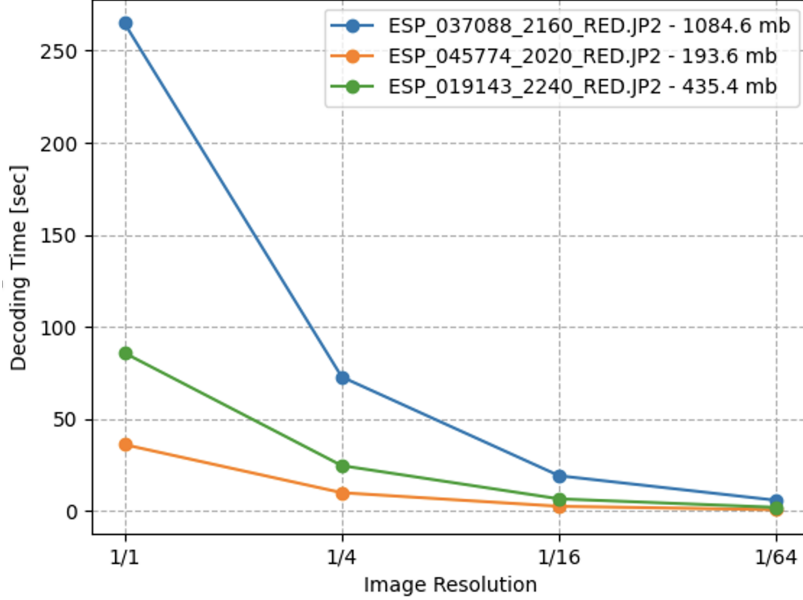


Figure 1. Decoding times of various JPEG2000 images in the HiRISE archive using a single thread on a 2.4 GHz 8-Core Intel Core i9 CPU. The decoding time improves if the image is opened at a lower resolution. However, a lower resolution may not always retain enough signal to noise for a computer vision algorithm to act reliably. The image size on disk is listed in the plot legend.

94 In order to automate the detection of landforms on the Martian surface we need a computer vision algorithm capable
 95 of learning the ideal features for detection. The advantage of a neural network is that it can be trained to identify
 96 subtle features inherent in a large data set. This learning capability is accomplished by allowing the weights and biases
 97 to vary in such a way as to minimize the difference (i.e. the cross entropy) between the output of the neural network
 98 and the expected or desired value from the training data. Our training data is separated into two classes; a generic
 99 ‘background’ class that represents most types of land and a ‘brain coral’ class for our terrain of interest. The training
 100 data is split in a 3:1 ratio for background to brain coral in order to provide a diverse range of background samples
 101 as needed to eliminate false positives from similar-looking terrain to brain coral (e.g. aeolian ridges or deflationary
 102 terrain). When we started this study, we only had two hand-labeled examples of brain coral and used active learning
 103 to build a more robust set of training data. Active learning requires iterating over our evaluations to eliminate false
 104 positives by adding to our training data for the background class along with adding true positives to the brain coral
 105 class. The full list of images used to generate training samples is listed in Table 1. It is important to train on a diverse
 106 population of background images since it needs to generalize to the ~50,000 images in the HiRISE archive. We trained
 107 multiple networks for our study and used the one with the best results. We found shrinking the input window size
 108 usually degrades performance below 128 pixels, therefore all of the classifier networks we tested have bigger window
 109 sizes (either 128, 256, or 512 pixels; see Table 2). The networks are trained on data between ~25-50 cm/px and
 110 supports the conclusion of other papers stating due to the convolutions and pooling operations the network is partially
 111 scale invariant (Xu et al. 2014; Xu et al. 2019; Wimmer et al. 2023). Obviously, if the brain coral feature is larger
 112 than the window size this conclusion breaks down and the network needs a larger input window. We generate training
 113 tiles using the map-projected satellite images and ignore portions of the image containing the black border. A subset
 114 of our brain coral training samples can be seen in Figure 2.

Table 1. Training Data

Name	Class	Description
ESP_016215_2190	Brain Coral	Area West of Erebus Montes
ESP_016287_2205	Brain Coral	Lineated Valley Floor Material in Terrain North of Arabia Region
ESP_018707_2205	Brain Coral	Candidate New Impact Site Formed between January 2010 and June 2010
ESP_022629_2170	Brain Coral	Lobate Deposits in Crater in Arabia Terra
ESP_042725_2210	Brain Coral	Lineated Valley Floor Material in Terrain North of Arabia Region
ESP_052675_2215	Brain Coral	Region Near Erebus Montes
ESP_057317_2210	Brain Coral	Crater with Preferential Ejecta Distribution on Possible Glacial Unit
ESP_061141_2195	Brain Coral	Candidate Landing Site for SpaceX Starship in Arcadia Region
PSP_001426_2200	Brain Coral	Lobate Apron Feature in Deuteronilus Mensae Region
PSP_007531_2195	Brain Coral	Striated Flows in Canyon
ESP_019385_2210	Brain Coral	Lineated Valley Floor Material in Terrain North of Arabia Region
ESP_036917_2210	Brain Coral	Doubly-Terraced Elongated Crater in Arcadia Planitia
ESP_052385_2205	Brain Coral	Sample Region Near Erebus Montes
ESP_055146_2220	Brain Coral	Candidate Recent Impact Site
ESP_060698_2220	Brain Coral	Subliming Ice
ESP_061075_2195	Brain Coral	Candidate Landing Site for SpaceX Starship in Arcadia Region
ESP_077488_2205	Brain Coral	Lineated Valley Floor Material in Terrain North of Arabia Region
PSP_001410_2210	Brain Coral	Impact Crater Filled with Layered Deposits
PSP_001466_2215	Brain Coral	Fretted Terrain Valleys and Apron Materials
PSP_009740_2200	Brain Coral	Debris Aprons in Eastern Erebus Montes
ESP_011428_2200	Background	Candidate New Impact Site Formed between January and October 2008
ESP_011571_2270	Background	Very Fresh Small Impact Crater
...
PSP_008158_1825	Background	Region North of Nicholson Crater
PSP_010346_1570	Background	Graben in Memnonia Fossae

NOTE—The full table consists of 149 images and is hosted online.

3. CROSS-VALIDATION AND ALGORITHM COMPARISON

A hybrid pipeline approach allows us to save processing time by evaluating data at a lower resolution while maintaining most of the accuracy compared to a full-resolution network. The hybrid approach starts with a classifier for quickly evaluating images followed by a segmentation network for full-resolution pixel-scale inference. Multiple classifiers were tested using different architectures and input sizes which leads to differences in accuracy and evaluation speed (see Table 2). We tested two types of classifiers, one in the Fourier domain in order to leverage blocks of coefficients from an encoding process similar to JPEG and a spatial classifier for comparison. Both classifiers work with data at 1/16 resolution. The spatial classifier uses a normalization layer in the network to transform the input to have a mean of 0 and a standard deviation of 1. The Fourier domain classifier uses the JPEG encoding processing to tile an input into 8x8 tiles and then applies a discrete cosine transform to each tile before being reshaped into a smaller but deeper block for the network (see Figure 3). The tiling and encoding process can transform an input image of 256x256 into a data cube of size 32x32x64. The smaller window size is advantageous in convolutional neural networks since the first layer of the network usually reduces the dimensionality in the number of channels from 64 to 32. Additionally, the smaller image size requires fewer operations per layer and speeds up inference whereas, with a similar architecture for the spatial data, the first layer increases the dimensionality of the input since there is only one channel pertaining to color instead of frequency. Early on in our study we started with random forests and multi-layer perceptrons but quickly found more benefit in using bigger input sizes which are better suited for convolutional networks. We found a negative correlation between the input size and the number of false positives with every algorithm we tested and ultimately

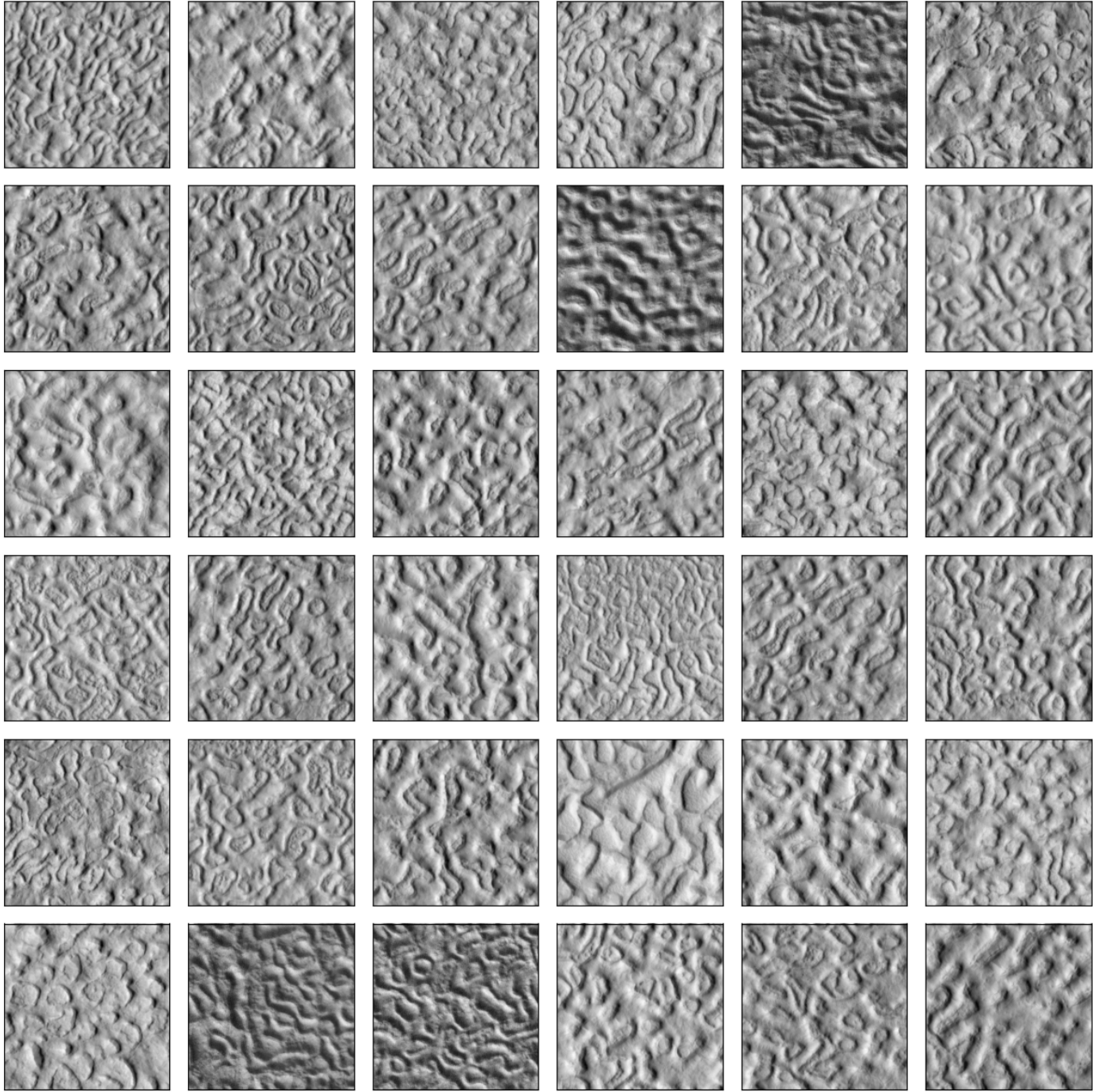


Figure 2. A mosaic of training samples for the brain coral class. Each tile shown here has a size of 512×512 pixels which corresponds roughly to $\sim 128 \times 128m^2$ area at the native resolution. The tiles shown here are reminiscent of the data used to train the segmentation algorithm. Although, images pertaining to the background class are not shown here. The brain coral terrain exhibits pitted mounds next to small ridges which range in size from 1-10 meters. Most of the examples shown here are open-cell brain coral terrain. Closed cell terrain can be found

settled on window sizes of 128x128 or 256x256, depending on the classifier. The advantage of using a smaller window size like 128x128 is that we can make more training data for a given set of HiRISE images (see Table 2).

The classifier network may be accurate and fast but it lacks the precision we need to make more detailed measurements of the surface. To detect brain coral at a scale smaller than a meter per pixel involves a network that can operate

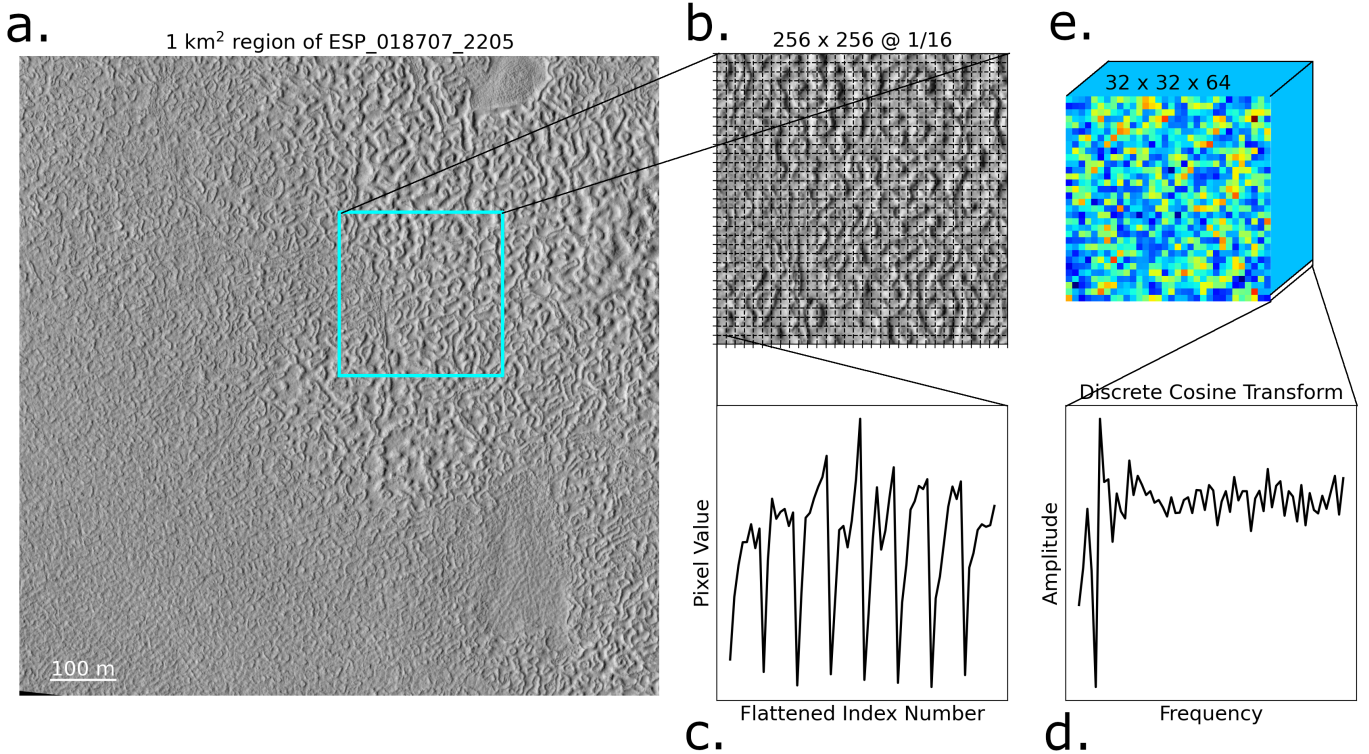


Figure 3. An overview of the inputs for each step in our processing pipeline. **a)** A region in the HiRISE image of ESP_018707_2205 is shown at the native resolution (0.3m/px) with a blue box highlighting the window size for our classifier network. **b)** A 256 x 256 pixel window is used as input for our spatial classifier algorithm however the window is at 1/16 the original resolution (1.2m/px). A grid of 8x8 squares is displayed showing that image gets tiled and preprocessed using parts of a JPEG encoder which involves the discrete cosine transform (**d**). **c)** A single 8x8 tile flattened into a 1d array which is used for the DCT transform (**d**). **e)** A block of Fourier coefficients is rearranged into a data cube and used as input for our Fourier classifier. Reducing the image size and ultimately the channel size after the first conv. layer significantly shortens the network's processing time compared to the spatial image input.

at the native image resolution for HiRISE (~0.25-0.5 m/pixel). We designed a custom U-net architecture based on MobileNetV3 in order to build a segmentation network for pixel-level predictions (Howard et al. 2019). We chose the MobileNet architecture due to its improved performance over other similar CNNs like Resnet or VGG (He et al. 2015). MobileNet maintains state of art accuracy on the CiFAR1000 test while requiring less training and energy consumption than the bigger CNNs (e.g. Resnet). Despite mobile being in the name, the network was designed for ARM-based processors which are growing in popularity due to their energy efficiency making them suitable devices for space-based operation (Dunkel et al. 2022). The U-net architecture is a popular choice for segmentation networks due to its ability to learn the context of the image and its ability to learn the boundaries of the objects in the image (Ronneberger et al. 2015; Garcia-Garcia et al. 2017). The U-net architecture consists of a contracting encoder path and an expanding decoder path that gives it a U-shaped architecture. The encoder path applies convolutions to downsample the input image and extract relevant features. The decoder path upsamples these features to produce a pixel-wise segmentation mask of the same size as the input image. Skip connections connect layers in the encoder and decoder at the same network depth, concatenating encoder features with upsampled decoder features. This allows the decoder layers to incorporate both lower-level features and higher-level context from the encoder, aiding precise localization and segmentation. The expanding path enables precise localization by propagating context information to higher-resolution layers.

Due to the size and complexity of the U-Net architecture, we found improved performance by training the network in multiple stages. First, the encoder portion of the U-Net was trained to predict low-resolution (32x32) segmentation masks from the input images (512x512). As shown by the jitter in testing accuracy (Figure 4), the encoder alone did not generalize adequately to the testing data. Next, the full U-Net was assembled by appending the decoder portion

157 and fixing the encoder weights. Only the decoder was trained, and conditioned on upscaling the low-resolution encoder
 158 outputs to the native image resolution. Skip connections from select encoder layers to decoder layers of equal depth
 159 were utilized, as per the U-Net design. Since the base network architecture (MobileNet) is not a U-Net, determining
 160 which layers to use for skip connections required empirical tuning. The number of upsampling layers in the decoder
 161 constrained possible skip connection sources in the encoder. Finally, end-to-end fine-tuning of the full U-Net was
 162 performed using a learning rate an order of magnitude lower than the previous training stages. The Adam optimizer
 163 was used for training, with binary cross-entropy loss, as there were only two classes of interest. A comparison of the
 164 classifier and segmentation network is in Figure 5.

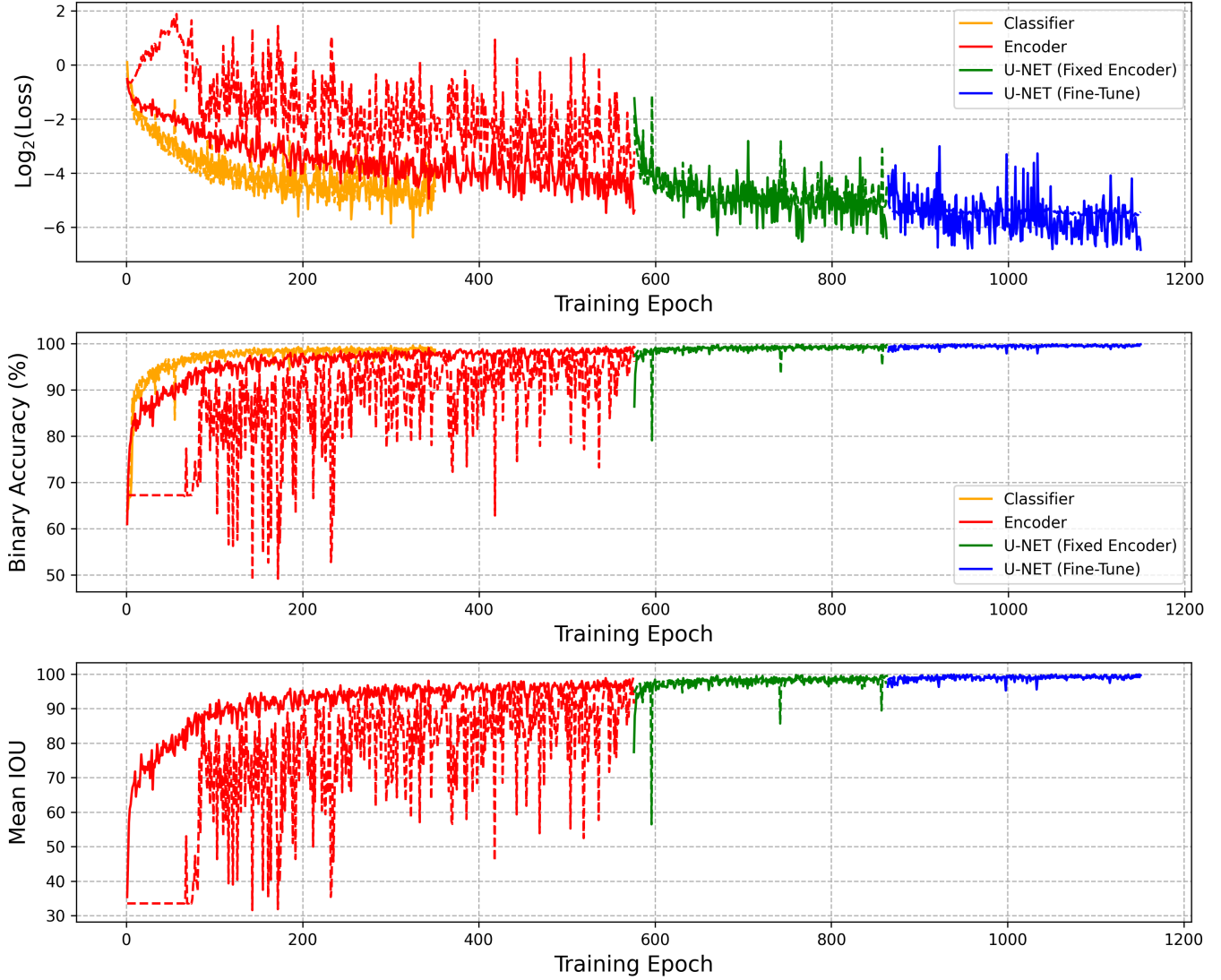


Figure 4. A plot comparing the training behavior for the networks used in our survey. The classifier leverages data in the fourier domain from a spatial image at 1/16 the original resolution. Whereas the U-net algorithm uses spatial data at the native resolution and a MobileNetV3 architecture. We found training the U-Net in pieces yielded better testing performance.

4. RESULTS AND DISCUSSION

165 The HiRISE camera on MRO has been acquiring data of the Martian surface for over a decade. We acquired a
 166 snapshot of the archive in 2021 when this part of a Mars Data Analysis Program (MDAP) began. Our local snapshot
 167 of the archive contains 52,618 images subtending over 28.1 TB of space on disk. We have a problem of needing to
 168

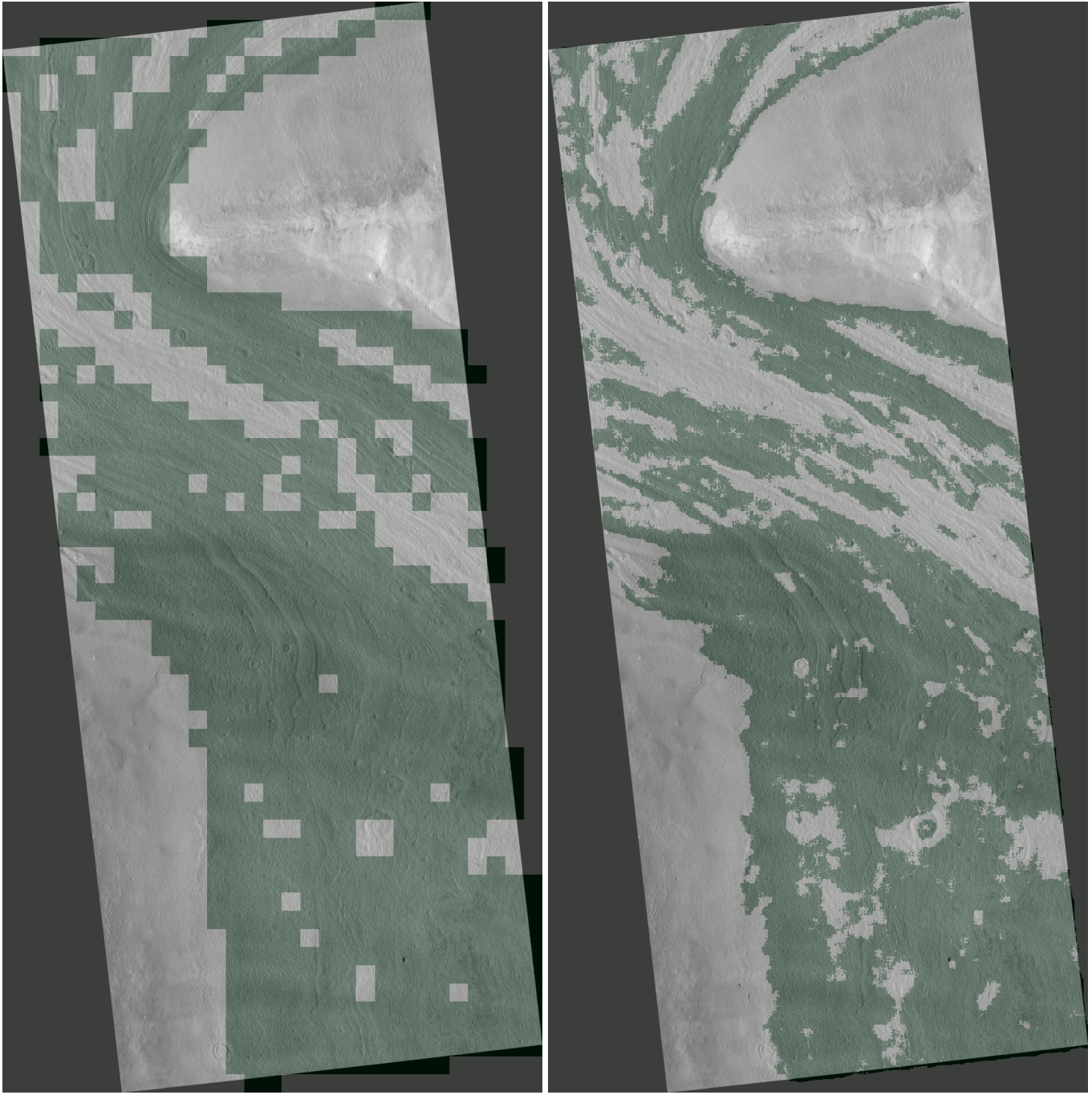


Figure 5. A comparison of outputs between our final classifier and segmentation network overlaid on the image *ESP_016287_2205*. **Left)** An output from our classifier corresponding to detections from the brain coral class. The pixelated output corresponds to the field of view for the classifier (~64x64 meter region). **Right)** A probability map from the segmentation network for the brain coral class. The brain coral is highlighted in red while the background is in blue. The boundaries are defined at the native resolution and on the pixel level using a U-NET.

169 find a rather rare terrain (likely covers <1% of the surface) over many images and it would be ideal to have pixel-level
 170 boundaries for measuring the extent (see Figure 6). Figure 1 shows the amount of time it takes to decode a single
 171 HiRISE image based on the decoding resolution and image size. The estimated time to decode the entire archive at
 172 the native resolution is about 170.3 hours and when we combine that with segmenting the dataset we get another ~
 173 145.4 hours. These numbers are based on interpolating the results of our algorithm based on image size and quantity.

Table 2. Network Performance

model name	Training Size	Testing Size	F1 Score	TP	TN	FP	FN	1Kx1K / sec
unet-512-spatial	58641	6516	0.998	99.8	99.7	0.2	0.3	6.5
cnn-128-spatial	58641	6516	0.996	99.6	99.6	0.4	0.4	33.9
resnet-128-spatial	58641	6516	0.995	99.7	99.4	0.6	0.3	21.7
cnn-256-spatial	11493	1277	0.991	99.2	99.0	1.0	0.8	46.4
resnet-256-spatial	13736	1527	0.990	99.6	98.5	1.5	0.4	35.1
MobileNet-128-spatial	58641	6516	0.988	98.6	99.0	1.0	1.4	97.7
MobileNet-256-spatial	13736	1527	0.977	96.0	99.5	0.5	4.0	169.0
cnn-256-dct	13736	1527	0.930	90.6	95.7	4.3	9.4	228.4
cnn-128-dct	58641	6516	0.912	90.4	92.1	7.9	9.6	134.2
resnet-256-dct	13736	1527	0.844	87.3	80.5	19.5	12.7	130.0
MobileNet-256-dct	13736	1527	0.836	93.6	69.6	30.4	6.4	159.8

NOTE—All metrics are computed using the test data. The last column represents how many 1K x 1K windows each model can process per second on a RTX 3090 GPU. The numbers in the model name represent the size of the input window in pixels. TP = True Positive, TN = True Negative, FP = False Positive, FN = False Negative.

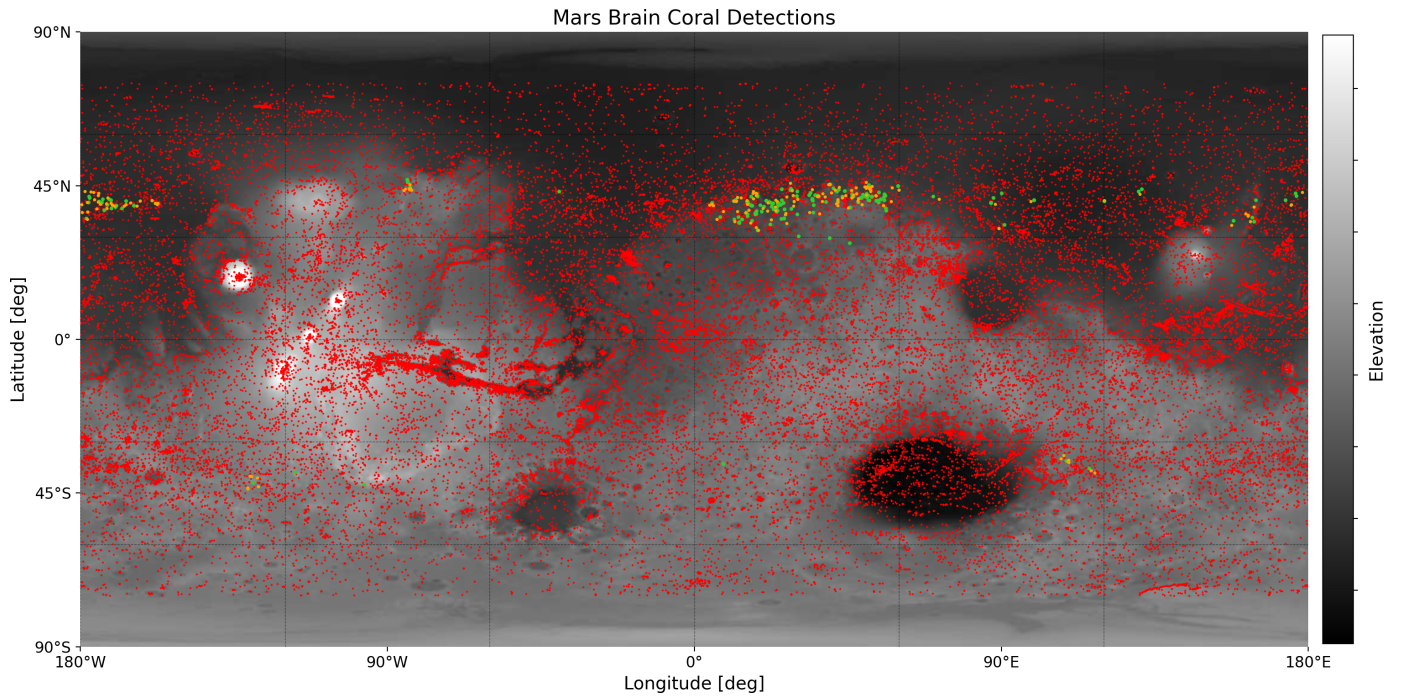


Figure 6. A map of candidate regions that contain Brain Coral plotted over elevation data. Our survey vetted 52,618 HiRISE images down to 456 candidates. Of those candidates, we manually vetted the results and found 201 positive detections, 189 false positives and 94 skeptical detections. The skeptical detections were difficult to discern due to image resolution, erosion or being confused with deflationary terrain. Green areas indicate positive brain coral, orange dots represent a “maybe” label and red means no brain coral is present. The elevation data is blended from the Mars Orbiter Laser Altimeter (MOLA), an instrument aboard NASA’s Mars Global Surveyor spacecraft (MGS), and the High-Resolution Stereo Camera (HRSC), an instrument aboard the European Space Agency’s Mars Express (MEX) spacecraft.

In total, the algorithm would take about 14 days to process the entire archive using the segmentation algorithm. Utilizing a hybrid pipeline approach with a classifier that operates on lower resolution data was proved to be $\sim 90\%$

as accurate as our segmentation algorithm. Since the classifier is about $15 \times$ faster than the segmentation network and we evaluate images at 1/16 resolution with it, we process the entire archive in ~ 21 hours.

The implications of identifying the processes responsible for the relatively young brain coral terrains on Mars are significant. If brain coral formed by freeze-thaw cycles similar to the processes that create patterned stone circles on Earth (Kessler et al. 2001; Kääb et al. 2014), it would imply that freeze-thaw processes redistribute the rock distributions near the martian surface. Therefore, it is critical to test the alternative hypotheses for brain coral formation using the available data. The hypotheses include sublimation lag (Mangold 2003), topographic inversion of polygons (Levy et al. 2009), and rock sorting akin to stone circles (Noe Dobrea et al. 2007). Observables that can evaluate these hypotheses include distribution, morphology, thermal inertia, rock density, crater statistics, and more. As the comprehensive analysis provides statistically significant data, conclusions about the genesis of brain coral will be possible. In a future study we will map rock distributions in HiRISE images using shadow measurements to derive rock size and abundance (Golombek et al. 2012; Huertas et al. 2006). This technique will produce spatial density maps showing variations in rock populations. Full rock resolvability is possible down to ~ 0.75 m diameter with HiRISE (Golombek et al. 2012). Meter-scale clasts do form stone circles on Earth (Gallagher et al. 2011) and if brain coral formed similarly, we would expect increased rock abundance on ridges and in the transition from open to closed terrain. Quantifying rock distribution will help test hypotheses related to possible cryoturbation and freeze-thaw processes in brain coral formation. Determining if brain coral formed via freeze-thaw cycles will reveal locations of past liquid water and inform astrobiological exploration targets seeking extant life.

5. CONCLUSION

We developed a hybrid pipeline using convolutional neural networks to automate the detection of rare brain coral terrain in a large dataset of 52,618 HiRISE images of Mars. A Fourier domain classifier on compressed imagery allowed rapid screening before pixel-level segmentation mapping of landform boundaries, enabling processing of the 28TB archive in just 21 hours rather than 14 days. This approach revealed 456 detections which was narrowed down to 201 positive confirmations after manually vetting the results. If brain coral morphology indicates freeze-thaw processes similar to stone circles on Earth (Kessler et al. 2001), it would confirm past liquid water availability and inform astrobiology site selection. Golombek et al. 2012's rock counting can map spatial variations in boulder populations from shadows, while future work by Pearson et al. (in prep.) will focus specifically on quantifying boulder density variation across brain coral using machine learning. Integrating multiple remote sensing datasets can provide robust tests of competing brain coral formation hypotheses and reveal insights into Mars' recent climate, geology, and potential habitability. Timely processing of big orbital data enables more extensive surveys to inform landing site selection and identify rare landforms for study.

6. ACKNOWLEDGEMENTS

The research described in this publication was carried out in part at the Jet Propulsion Laboratory, California Institute of Technology, under a contract with the National Aeronautics and Space Administration. This research has made use of the High Resolution Imaging Science Experiment on the Mars Reconnaissance Orbiter, under contract with the National Aeronautics and Space Administration. We acknowledge funding support from the National Aeronautics and Space Administration (NASA) Mars Data Analysis Program (MDAP) Grant Number NNN19ZDA001N.

REFERENCES

- 213 Balme, M., Gallagher, C., Page, D., Murray, J., & Muller, J.-P. 2009, Icarus, 200, 30, doi: <https://doi.org/10.1016/j.icarus.2008.11.010>
- 214 Carr, M. H. 2001, J. Geophys. Res., 106, 23571, doi: [10.1029/2000JE001316](https://doi.org/10.1029/2000JE001316)
- 215 Chamain, L. D., & Ding, Z. 2019, arXiv e-prints, arXiv:1909.05638, doi: [10.48550/arXiv.1909.05638](https://doi.org/10.48550/arXiv.1909.05638)
- 216 Costard, F., Forget, F., Mangold, N., & Peulvast, J. P. 2002, Science, 295, 110, doi: [10.1126/science.1066698](https://doi.org/10.1126/science.1066698)
- 217 Dai, Y., Zheng, T., Xue, C., & Zhou, L. 2022, Remote Sensing, 14, doi: [10.3390/rs14246297](https://doi.org/10.3390/rs14246297)
- 218 Dalal, N., & Triggs, B. 2005, in 2005 IEEE Computer Society Conference on Computer Vision and Pattern Recognition (CVPR'05), Vol. 1, 886–893 vol. 1, doi: [10.1109/CVPR.2005.177](https://doi.org/10.1109/CVPR.2005.177)

- 228 Dunkel, E., Swope, J., Towfic, Z., et al. 2022, in IGARSS
 229 2022 - 2022 IEEE International Geoscience and Remote
 230 Sensing Symposium, 5301–5304,
 231 doi: [10.1109/IGARSS46834.2022.9884906](https://doi.org/10.1109/IGARSS46834.2022.9884906)
- 232 Gallagher, C., Balme, M., Conway, S., & Grindrod, P. 2011,
 233 Icarus, 211, 458,
 234 doi: <https://doi.org/10.1016/j.icarus.2010.09.010>
- 235 Garcia-Garcia, A., Orts-Escalano, S., Oprea, S.,
 236 Villena-Martinez, V., & Garcia-Rodriguez, J. 2017, arXiv
 237 e-prints, arXiv:1704.06857,
 238 doi: [10.48550/arXiv.1704.06857](https://doi.org/10.48550/arXiv.1704.06857)
- 239 Goldthwait, R. P. 1976, Quaternary Research, 6, 27,
 240 doi: [https://doi.org/10.1016/0033-5894\(76\)90038-7](https://doi.org/10.1016/0033-5894(76)90038-7)
- 241 Golombek, M., Huertas, A., Kipp, D., & Calef, F. 2012,
 242 International Journal of Mars Science and Exploration, 7,
 243 1, doi: [10.1555/mars.2012.0001](https://doi.org/10.1555/mars.2012.0001)
- 244 Gueguen, L., Sergeev, A., Kadlec, B., Liu, R., & Yosinski,
 245 J. 2018, in Advances in Neural Information Processing
 246 Systems, ed. S. Bengio, H. Wallach, H. Larochelle,
 247 K. Grauman, N. Cesa-Bianchi, & R. Garnett, Vol. 31
 248 (Curran Associates, Inc.).
https://proceedings.neurips.cc/paper_files/paper/2018/file/7af6266cc52234b5aa339b16695f7fc4-Paper.pdf
- 251 Hallet, B., & Waddington, E. 2020, Buoyancy Forces
 252 Induced by Freeze-thaw in the Active Layer: Implications
 253 for Diapirism and Soil Circulation, 251–279,
 254 doi: [10.4324/9781003028901-11](https://doi.org/10.4324/9781003028901-11)
- 255 He, K., Zhang, X., Ren, S., & Sun, J. 2015, arXiv e-prints,
 256 arXiv:1512.03385, doi: [10.48550/arXiv.1512.03385](https://doi.org/10.48550/arXiv.1512.03385)
- 257 Howard, A., Sandler, M., Chu, G., et al. 2019, arXiv
 258 e-prints, arXiv:1905.02244,
 259 doi: [10.48550/arXiv.1905.02244](https://doi.org/10.48550/arXiv.1905.02244)
- 260 Huertas, A., Cheng, Y., & Madison, R. 2006, 2006 IEEE
 261 Aerospace Conference, 14 pp.
<https://api.semanticscholar.org/CorpusID:20565326>
- 262 Ioffe, S., & Szegedy, C. 2015, arXiv e-prints,
 263 arXiv:1502.03167, doi: [10.48550/arXiv.1502.03167](https://doi.org/10.48550/arXiv.1502.03167)
- 264 Kääb, A., Girod, L., & Berthling, I. 2014, The Cryosphere,
 265 8, 1041, doi: [10.5194/tc-8-1041-2014](https://doi.org/10.5194/tc-8-1041-2014)
- 266 Kessler, M. A., Murray, A. B., Werner, B. T., & Hallet, B.
 267 2001, Journal of Geophysical Research: Solid Earth, 106,
 268 13287, doi: <https://doi.org/10.1029/2001JB000279>
- 269 Kessler, M. A., & Werner, B. T. 2003, Science, 299, 380,
 270 doi: [10.1126/science.1077309](https://doi.org/10.1126/science.1077309)
- 271 Konrad, J.-M., & Morgenstern, N. R. 1980, Canadian
 272 Geotechnical Journal, 17, 473, doi: [10.1139/t80-056](https://doi.org/10.1139/t80-056)
- 273 Kreslavsky, M. A., Head, J. W., & Marchant, D. R. 2008,
 274 Planet. Space Sci., 56, 289, doi: [10.1016/j.pss.2006.02.010](https://doi.org/10.1016/j.pss.2006.02.010)
- 275 Levy, J. S., Head, J. W., & Marchant, D. R. 2009, Icarus,
 276 202, 462,
 277 doi: <https://doi.org/10.1016/j.icarus.2009.02.018>
- 278 Malin, M. C., & Edgett, K. S. 2001, J. Geophys. Res., 106,
 279 23429, doi: [10.1029/2000JE001455](https://doi.org/10.1029/2000JE001455)
- 280 Mangold, N. 2003, Journal of Geophysical Research
 281 (Planets), 108, 8021, doi: [10.1029/2002JE001885](https://doi.org/10.1029/2002JE001885)
- 282 —. 2005, Icarus, 174, 336, doi: [10.1016/j.icarus.2004.07.030](https://doi.org/10.1016/j.icarus.2004.07.030)
- 283 McEwen, A. S., Eliason, E. M., Bergstrom, J. W., et al.
 284 2007, Journal of Geophysical Research (Planets), 112,
 285 E05S02, doi: [10.1029/2005JE002605](https://doi.org/10.1029/2005JE002605)
- 286 McEwen, A. S., Ojha, L., Dundas, C. M., et al. 2011,
 287 Science, 333, 740, doi: [10.1126/science.1204816](https://doi.org/10.1126/science.1204816)
- 288 Milliken, R. E., Mustard, J. F., & Goldsby, D. L. 2003,
 289 Journal of Geophysical Research (Planets), 108, 5057,
 290 doi: [10.1029/2002JE002005](https://doi.org/10.1029/2002JE002005)
- 291 Nagle-McNaughton, T., McClanahan, T., & Scuderi, L.
 292 2020, Remote Sensing, 12, doi: [10.3390/rs12213607](https://doi.org/10.3390/rs12213607)
- 293 Noe Dobrea, E. Z., Asphaug, E., Grant, J. A., Kessler,
 294 M. A., & Mellon, M. T. 2007, in LPI Contributions, Vol.
 295 1353, Seventh International Conference on Mars, ed. LPI
 296 Editorial Board, 3358
- 297 Palafox, L. F., Hamilton, C. W., Scheidt, S. P., & Alvarez,
 298 A. M. 2017, Computers and Geosciences, 101, 48,
 299 doi: <https://doi.org/10.1016/j.cageo.2016.12.015>
- 300 Qiu, D., Rothrock, B., Islam, T., et al. 2020, Planetary and
 301 Space Science, 188, 104943,
 302 doi: <https://doi.org/10.1016/j.pss.2020.104943>
- 303 Ronneberger, O., Fischer, P., & Brox, T. 2015, arXiv
 304 e-prints, arXiv:1505.04597,
 305 doi: [10.48550/arXiv.1505.04597](https://doi.org/10.48550/arXiv.1505.04597)
- 306 Russakovsky, O., Deng, J., Su, H., et al. 2015, International
 307 Journal of Computer Vision, 115, 211,
 308 doi: [10.1007/s11263-015-0816-y](https://doi.org/10.1007/s11263-015-0816-y)
- 309 Squyres, S. W. 1978, Icarus, 34, 600,
 310 doi: [10.1016/0019-1035\(78\)90048-9](https://doi.org/10.1016/0019-1035(78)90048-9)
- 311 Taber, S. 1929, Journal of Geology, 37, 428,
 312 doi: [10.1086/623637](https://doi.org/10.1086/623637)
- 313 —. 1930, Journal of Geology, 38, 303, doi: [10.1086/623720](https://doi.org/10.1086/623720)
- 314 Trombotto, D. 2000, Revista do Instituto Geológico, 21, 33,
 315 doi: [10.5935/0100-929X.20000004](https://doi.org/10.5935/0100-929X.20000004)
- 316 Wagstaff, K. L., Lu, Y., Stanboli, A., et al. 2018, in
 317 Proceedings of the Thirty-Second AAAI Conference on
 318 Artificial Intelligence and Thirtieth Innovative
 319 Applications of Artificial Intelligence Conference and
 320 Eighth AAAI Symposium on Educational Advances in
 321 Artificial Intelligence, AAAI'18/IAAI'18/EAAI'18
 322 (AAAI Press)
- 323 Werner, B. T. 1999, Science, 284, 102,
 324 doi: [10.1126/science.284.5411.102](https://doi.org/10.1126/science.284.5411.102)

- 326 Williams, G. D., Powell, C. M., & Cooper, M. A. 1989,
327 Geological Society of London Special Publications, 44, 3,
328 doi: [10.1144/GSL.SP.1989.044.01.02](https://doi.org/10.1144/GSL.SP.1989.044.01.02)
- 329 Wimmer, T., Golkov, V., Dang, H. N., et al. 2023, arXiv
330 e-prints, arXiv:2304.05864,
331 doi: [10.48550/arXiv.2304.05864](https://doi.org/10.48550/arXiv.2304.05864)
- 332 Xu, X., Wang, G., Sullivan, A., & Zhang, Z. 2019, arXiv
333 e-prints, arXiv:1909.00114,
334 doi: [10.48550/arXiv.1909.00114](https://doi.org/10.48550/arXiv.1909.00114)
- 335 Xu, Y., Xiao, T., Zhang, J., Yang, K., & Zhang, Z. 2014,
336 arXiv e-prints, arXiv:1411.6369,
337 doi: [10.48550/arXiv.1411.6369](https://doi.org/10.48550/arXiv.1411.6369)